RESEARCH ARTICLE
SPACE PHYSICS: IONOSPHERIC PHYSICS

Earth and Planetary Physics
9: 400–409, 2025
doi: 10.26464/epp2024077

Evaluation of the satellite's wake effect on the electric field detector onboard the CSES-01 satellite

JianPing Huang[1,3], ZongYu Li[1,2,3*], Zhong Li[3], XingHong Zhu[4], JunGang Lei[5], YuanQing Miao[6], and WenJing Li[1]

[1]National Institute of Natural Hazards, Ministry of Emergency Management of China, Beijing 100085, China;

[2]School of Information Engineering, Qingdao Institute of Technology, Qingdao 266300, China;

[3]Institute of Intelligent Emergency Information Processing, Institute of Disaster Prevention, Langfang Hebei 065201, China;

[4]China Satellite Communications Co. Ltd., Beijing 100190, China;

[5]Lanzhou Institute of Physics, Lanzhou 730000, China;

[6]DFH Satellite Co. Ltd., Beijing 100094, China

Key Points:

- The disturbance from probe B of the electric field detector (EFD) is unrelated to the boom layout, and the plasma wake effect on the EFD spherical probes is negligible.
- The application of convolutional neural network-based data jump detection demonstrates probe B's consistent performance.
- The vector data from the EFD effectively reflect the spatial electromagnetic disturbance information.

Citation: Huang, J. P., Li, Z. Y., Li, Z., Zhu, X. H., Lei, J. G., Miao, Y. Q., and Li, W. J. (2025). Evaluation of the satellite's wake effect on the electric field detector onboard the CSES-01 satellite. *Earth Planet. Phys.*, *9*(2), 400–409. http://doi.org/10.26464/epp2024077

Abstract: This study aimed to evaluate the wake effect on the electric field detector (EFD) onboard the China Seismo-Electromagnetic Satellite (CSES-01). Through a series of experiments and analyses, we confirmed that the disturbance phenomenon from probe B of the EFD is not caused by the boom layout. To validate and determine whether it is influenced by the wake effect, we conducted two experiments. In the first experiment, the entire satellite platform underwent a 90° counterclockwise yaw maneuver to allow probe B to avoid the plasma wake region. We then verified whether the disturbance was improved. In the second experiment, the satellite platform performed a 180° counterclockwise yaw maneuver, positioning probe B on the ram side of the satellite and completely avoiding all satellite wakes. The plasma wake effect of the satellite did not significantly influence the spherical probes of the EFD because the measurement accuracy stayed relatively stable under the two experiments, despite the observed abnormalities in the operating state of spherical probe B. This consistency in performance is important for electric field detection missions because the spatial electric field vector data obtained from these probes continue to effectively reflect information on spatial electromagnetic disturbances. These two experimental results showed that probe B consistently exhibited data jump phenomena under various maneuver states, whereas probes A, C, and D did not display such phenomena in any maneuver state.

Keywords: CSES-01; payload; electric field detector; satellite attitude; data quality

1. Introduction

Entering the 21st century, multiple countries have launched low Earth orbit satellites specifically for monitoring changes in the space environment. For example, some satellites were launched with the main purpose of observing changes in spatial electromagnetic fields related to earthquake occurrences, such as France's DEMETER (Detection of Electro-Magnetic Emissions Transmitted from Earthquake Regions) satellite (Berthelier et al., 2006), the United States' QuakeSat satellite (Ukhorskiy et al., 2010), Russia's Predvestnik-E and Compass-II satellites (Fuselier and Lewis, 2011), and the China Seismo-Electromagnetic Satellite (CSES-01; Shen XH et al., 2018). According to observations from these satellite missions, substantial progress has been made in understanding the space plasma environment and its disturbances related to natural or artificial events, such as earthquakes, intense geomagnetic storm activities, and solar proton events. Zhima ZR et al. (2022a) reported the possible seismic ionospheric disturbances recorded by the CSES-01 by multistep data preprocessing and analysis methods using CSES-01 and multisource satellite and ground data. Yang YY et al. (2020) analyzed the in-flight performance of the CSES-01 payloads during an intense geomagnetic storm on August 25, 2018. They confirmed the measuring capabilities of the payloads by comparing magnetic field data with Swarm satellite observations. Zhima ZR et al. (2020) analyzed rising-tone quasiperiodic emissions observed by the CSES, which were associated with precipitating electrons in the inner radiation

First author: J. P. Huang, jianpinghuang@ninhm.ac.cn
Correspondence to: Z. Y. Li, lizongyu2021@163.com
Received 01 APR 2024; Accepted 14 OCT 2024.
First Published online 28 NOV 2024.

belt or the ultra low frequency (ULF) waves. The study confirmed that these quasiperiodic whistler waves could effectively scatter electrons into the atmosphere near the loss cone.

Space plasma is an essential material state in cosmic space, and its uneven distribution and disturbance effect on aerospace electronic equipment are critical components of space environment research (Wang L and Qin XG, 2002; Yang F et al., 2011). The spacecraft operating in different orbits can be affected by various factors, such as the space plasma and photoelectric effect, resulting in the deposition of charges on the spacecraft surface. As surface charges accumulate and reach the breakdown threshold, electrostatic discharge occurs, triggering a charging and discharging effect on the spacecraft surface and posing potential threats to its normal operation and safety (Jiang CH and Zhao ZY, 2008; Tian LC et al., 2012; Liu SH et al., 2019). The wake effect, characterized by a depleted ion density region behind the trajectory of the spacecraft resulting from velocity discrepancies between satellite and ambient plasma, generates a negative potential effect (Yuan QY and Sun WY, 2015). Using particle simulation, Bi JY and Li L (2018) found that the size of the spacecraft substantially affected the wake structure and charging, and the larger the platform, the more extensive was the wake effect that occurred. Additionally, Yang J et al. (2010) investigated the interaction of the spacecraft with ambient plasma by using satellite data, which revealed a peach-shaped plasma sheath and ion-depleted regions in the wake.

In such low Earth orbit environments, the supersonic velocities of satellites relative to the ambient plasma create a nonnegligible ion-depleted wake that modifies plasma properties, potentially interfering with the electromagnetic and plasma measurement instruments, and ultimately affecting the precision of scientific observations. To cross-calibrate the consistency of three electromagnetic field payloads onboard CSES-01, namely, the High Precision Magnetometer (HPM), Search-Coil Magnetometer (SCM), and Electric Field Detector (EFD, in this study), Zhima ZR et al. (2022b) proposed a method for synchronizing the waveform data sampling time between the electromagnetic field detection payloads. This approach ensured consistency within the overlapping detection frequency range across the three payloads and provided valuable insights for similar electromagnetic detection schemes in low Earth orbit satellites. Yang DH et al. (2022) evaluated the stability of very low frequency (VLF) band detection by verifying the systematic sampling time difference between the SCM and EFD under the VLF burst mode based on 3 years of data. Their findings revealed that the sampling time difference between the EFD and SCM remained predominantly below 0.5 s throughout a 3-year operational period, indicating good on-orbit stability for both the EFD and SCM. Diego et al. (2021) validated measurements of the EFD onboard CSES-01 by analyzing its responses to geomagnetic, plasma, and electromagnetic inputs. The theoretical model showed good agreement under average conditions but limited reliability for strong electric fields. Both natural and artificial signals were reliably detected by the EFD across various frequency bands. Consolini et al. (2021) analyzed 3D electric field fluctuations in the polar ionosphere via CSES-01 and found varying levels of multifractality (irregular patterns at different scales) near the polar cap and aurora, which they linked to particle precipitation. They also suggested a connection between these fluctuations and filamentation of field-aligned current. Space exploration indicated that ongoing observations of multiple targets could lead to statistically significant results and that the space EFD was essential for seismic detection (Liu Z et al., 2021).

Our team analyzed the jump classification of the three components of the electric field in the extremely low frequency (ELF) band based on EFD data from CSES-01 and found that spherical probe B located at the tail of the satellite was significantly different from the other probes, which was suspected to be related to the wake effect of the satellite platform (Huang JP et al., 2023). To confirm the working status of probe B and the possibility of a wake effect, we conducted further analyses based on observation data of the satellite's yaw maneuver experiment in orbit, with the aim of ascertaining the working conditions of probe B and the influence of the wake effect on the satellite platform.

2. Payload and Methods

2.1 The EFD Onboard CSES-01

The EFD was designed for the detection of spatial electric fields within the context of a spatial plasma environment. It serves as one of the primary payloads on CSES-01. The EFD works on the passive double-probe detection principle by acquiring both local and global spatial electric field data along the orbit of the satellite. The data provide a foundation for scientific research, especially for the extraction of variations in the electromagnetic fields associated with earthquake generation and their underlying perturbation mechanisms. The CSES-01 uses the CAST2000 satellite platform, and according to the technological status of the platform and the requirements of the scientific objective, as well as the fundamental characteristics of the Earth's ionospheric spatial electric field, the EFD selected a double-probe detection technology scheme. On the satellite are four 4.5-m-long booms, with 60-mm-diameter coated spheres (labeled A, B, C, and D, respectively) at their tips, forming a tetrahedral structure, as illustrated in Figure 1, which minimizes electromagnetic interference from the satellite on the payload. This configuration enhances the sensitivity and accuracy of the EFD, allowing for precise measurements of the spatial electric field in various environments (Huang JP et al., 2018b).

The electric field strength of the spatial vector can be determined by measuring the electrical potentials of the four spherical probes and subsequently calculating the potential differences between probes A and B, C and D, and A and D, along with the distances between them. Specifically, we considered the X, Y, and Z directions of the satellite platform, where X represents the direction of satellite flight (i.e., the front side), Z is the direction from the satellite platform to the Earth, and Y is the direction of Z crossed with X. Probe B is positioned at the rear side of the spacecraft during the standard flight mode of CSES-01. The EFD was specifically designed to measure the strengths of the electric field component across a broad frequency range, spanning from direct current (DC) up to 3.5 MHz. The frequency bands of the EFD were divided into the ULF band of DC to 16 Hz, the ELF band of 6 to 2.2 kHz, the VLF band of 1.8 to 20 kHz, and the high frequency (HF) band of 18 kHz

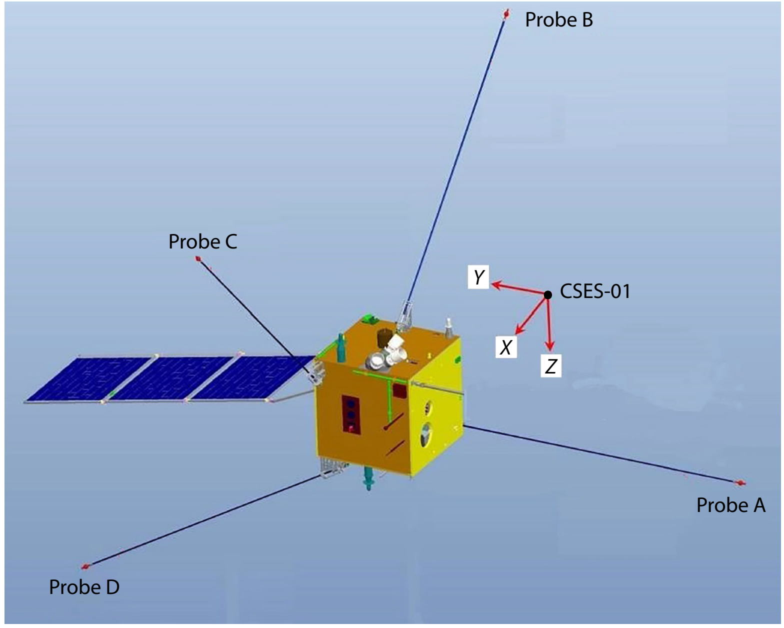

Figure 1. Configuration of the EFD's spherical probes onboard CSES-01 and extension rods.

to 3.5 MHz (Huang JP et al., 2018a; Ma MJ et al., 2018; Hu YP et al., 2020). This versatility allowed the EFD to accurately capture the electric field fluctuations across broad frequency bands, which is essential for studying various plasma phenomena and their associated electromagnetic effects in space.

2.2 Convolutional Neural Network-based Detection Method

The convolutional neural network (CNN) is one of the most widely used and representative multilayer neural network architectures in deep learning. Compared with traditional neural network models, the CNN has been optimized for the characteristics of input data, such as images and audio, enabling better feature extraction and achieving high accuracy in recognition and classification (Bai YD et al., 2021; Kavitha et al., 2022). They are widely applied in areas such as image classification, object detection and behavior recognition, and semantic segmentation. Different application tasks often require networks with different structures, such as AlexNet, LeNet, VGGNet, and ResNet (Zeiler and Fergus, 2014; He KM et al., 2016; Krizhevsky et al., 2017).

From the EFD's measurements in the ELF frequency band, we found that two types of data jumps exist: "straight-down" and "gradual-up" jumps, as illustrated in Figure 2. Automated detection and recognition of those phenomena can be achieved based on the CNN algorithm (Huang JP et al., 2023). For two adjacent data packets, a and b, we can use the following mathematical definitions to determine the types of connections between them:

Let M_a and M_b be the mean values of data packets a and b, respectively, whereas S_a and S_b are their variances, and K_a and K_b are their respective slopes.

(1) If $|M_a - M_b| > 3S_a$, then the type of jump connection between a and b is a straight-down jump.
(2) If $|M_a - M_b| \leq 3S_a$:
(i) If $K_a \times K_b > 0$, then the type of jump connection between a and b is a gradual-up jump;
(ii) If $K_a \times K_b < 0$, then the type of jump connection between a and b is a straight-down jump.

In this study, we used standard kernels of 5 × 5 and 3 × 3 sizes.

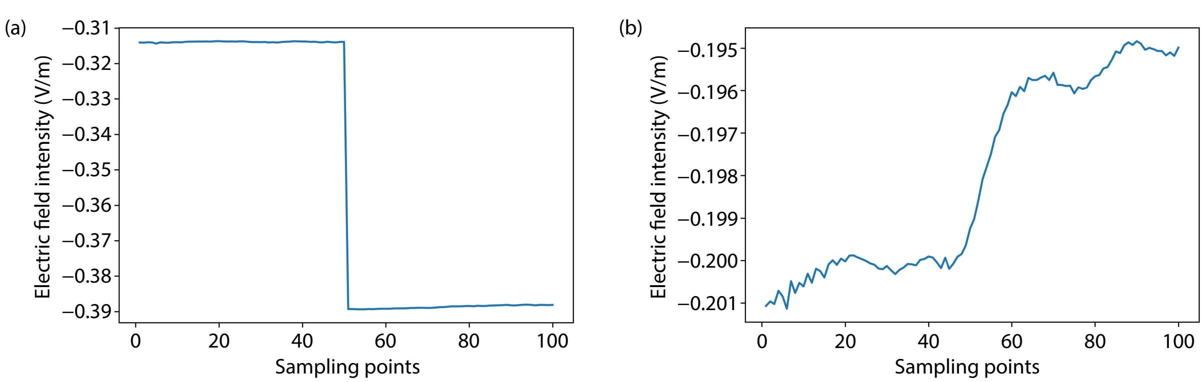

Figure 2. Two types of data jump phenomena in the waveform data observed by the EFD recorded in the ELF band: (a) a straight-down jump and (b) a gradual-up jump.

Specifically, 96 kernels of 5 × 5 were used in the first and second layers, whereas 256 kernels of 3 × 3 were ultimately integrated in the third layer. To extract hierarchical features in the convolutional layers while maintaining the spatial resolution of the input images, zero-padding was adopted to ensure consistent spatial dimensions for the input and output feature maps throughout the network. This process allowed us to preserve the original input image size within the network while still extracting increasingly abstract representations from each subsequent layer. To optimize the model, cross-validation was applied during training to determine the best combination of hyperparameters. The average accuracy of the model on the test set was calculated, and the hyperparameter combination that yielded the highest accuracy was selected as the final training parameter for the model. The sample set was manually screened from the ELF band between November 2019 and November 2020, with 1000 samples in each category, of which 900 were used for training and 100 for testing. The receiver operating characteristic (ROC) curve indicated that the CNN-based data jump detection method achieved high-precision detection and recognition in classification, with the area under the curve (AUC) metrics exceeding 90%. The specific details of the methodology can be found in Huang JP et al. (2023). To further trace the origins of data jumps, we continued to use this model for research and analysis.

2.3 Experiment Design

To further explore the influence of the wake effect on the accuracy of EFD measurements, the experimental verification was carried out by the entire satellite platform. Under the standard flight mode of CSES-01, probe B of the EFD was directly positioned at the rear of the spacecraft. Factually, the satellite's yaw maneuver can be used to reposition probe B to various directions on the platform. This allowed us to assess its exposure to plasma wake disturbances by comparison with different directions. Thus, we designed the on-orbit experiments in two yaw states to verify probe B, as listed in Table 1. We could investigate and observe the changes in satellite attitude and the positional variations of probe B under different yaw conditions based on the experimental design outlined in Table 1.

First, we conducted a test of the entire satellite's counterclockwise 90° yaw maneuver. The experimental results showed that this maneuver effectively positioned probe B away from the plasma wake region; thus, we could verify the improvement in the disturbed state. Subsequently, a counterclockwise 180° yaw maneuver was performed on the entire satellite, and the results indicated that under this yaw maneuver, probe B could be completely positioned on the front of the satellite, thus entirely avoiding all satellite wakes. To ensure the safety of the experiment, various safety risks associated with the satellite were thoroughly considered during the experimental process. These risks included, but were not limited to, attitude control system risks, satellite–ground link safety risks, and energy safety risks. The experiment was completed through a comprehensive assessment and control of these risks. In addition, the experimental states were analyzed and discussed in detail. According to the state of the satellite (as shown in Figure 3), observations were made regarding the satellite attitude changes and the positional variations of probe B under different experimental conditions.

As shown in Figure 3, the satellite achieved evasion of probe B through a counterclockwise 90° yaw maneuver, thereby verifying that the disturbed state had improved. This maneuver allowed probe B to avoid the plasma wake region, preventing potential interference and impact. Furthermore, when the entire satellite performed a 180° yaw maneuver, probe B was positioned on the ram-facing surface of the satellite, completely avoiding all satellite wakes.

3. Analysis

On December 25, 2018, we executed a data block injection to the satellite for a 90° yaw orbit maneuver mode (Orbit 4956). On December 26, we performed a data block injection to the satellite for a 180° yaw orbit maneuver mode (Orbit 4972). After successful injection of the data block, it was evident that both the attitude control system and the propulsion system of the satellite were functioning properly, providing a solid foundation for subsequent flight.

3.1 Statistical Analysis of Data Jumps

To investigate and analyze the statistical characteristics of data jumps in waveform data of the EFD, data from Orbits 4954 (normal), 4956 (counterclockwise rotation of 90°), and 4972 (rotation of 180°), which were recorded from December 25 to 26, 2018, were selected for comparison. The orbit trajectories are shown in Figure 4.

According to the statistical results presented in Figure 5, from the selected three-orbit data, one can see that probe B exhibited the most data jump events compared with the other three probes. Most important, no notable differences were observed between the experimental and normal states. Probes A, C, and D did not show significant changes in data jump characteristics. As illustrated in Figure 5, none of the probes underwent apparent disturbances (with probe A located within the satellite's ion wake region during the 90° yaw maneuver, and probe C positioned similarly to probe

Table 1. Experimental design of the satellite platform rotation.

Status	Probe B position	Time	Orbit number	Tail probe
Normal State	In the wake region	Day 1 03:10:25–03:45:00	4954	B
Experimental State 1	Outside the wake region, on the right side of the satellite	Day 1 06:19:53–06:54:28	4956	A
Experimental State 2	Far away from the wake region, in the front region of the satellite	Day 2 07:35:39–08:10:14	4972	C

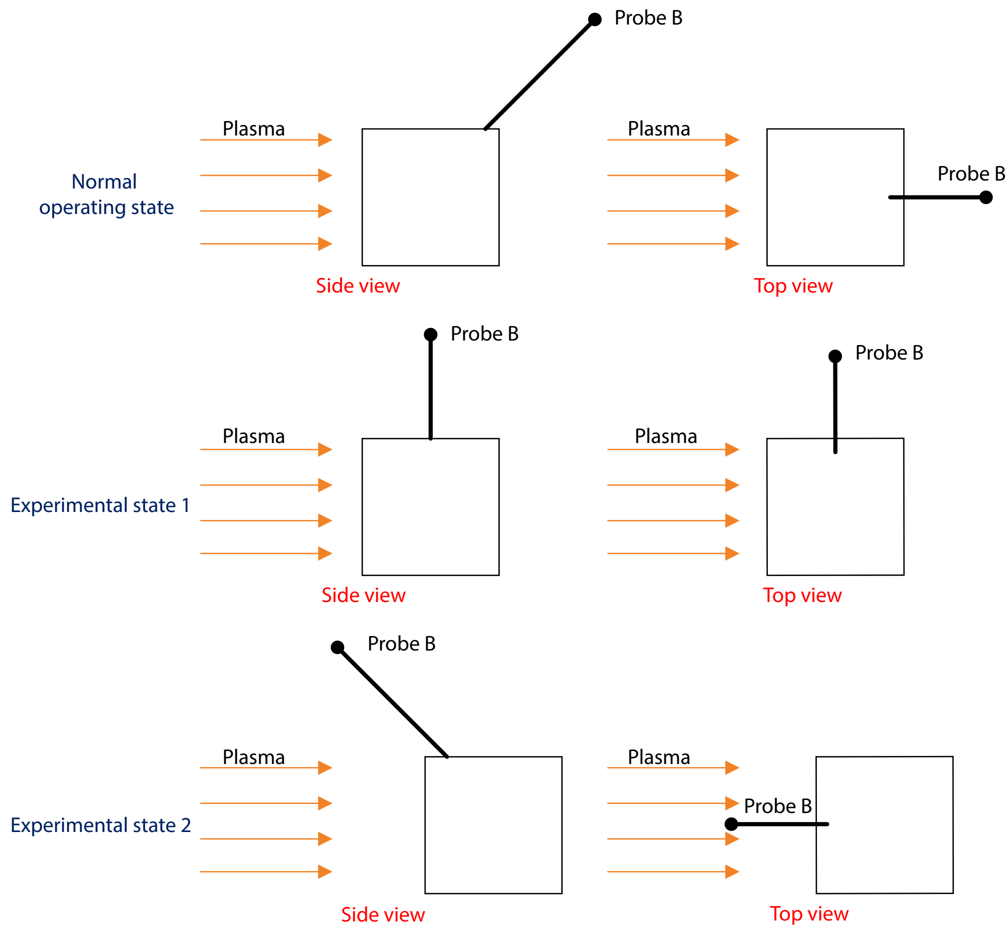

Figure 3. Diagram of the satellite position under the three conditions listed in Table 1.

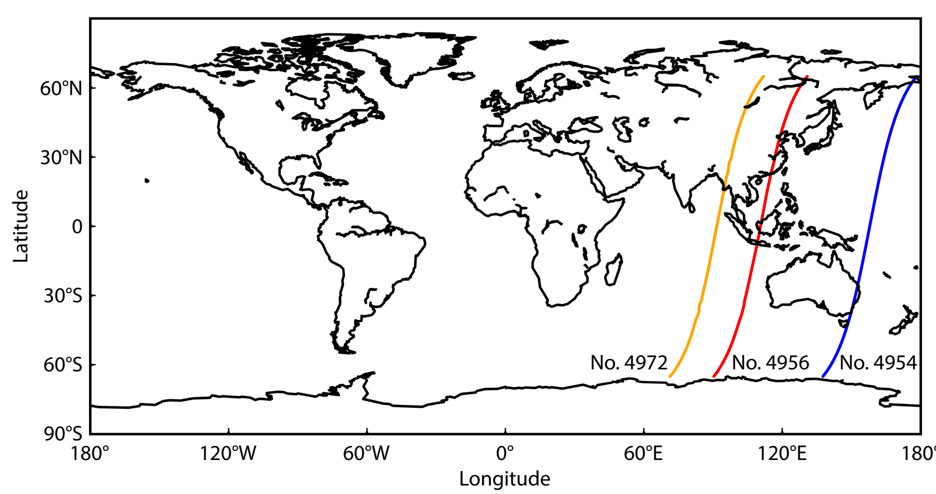

Figure 4. Satellite orbit diagram, with blue representing Orbit 4954, red representing Orbit 4956, and yellow representing Orbit 4972.

B during the normal flight when the 180° yaw maneuver was performed). Probe B consistently exhibited data jump phenomena across various maneuver states, whereas probes A, C, and D did not display noticeable data jump phenomena in any maneuver state. Further statistical analysis of the quantity characteristics of the gradual-up and straight-down types across the three orbits is presented in Figure 6.

Figure 6 presents the statistical distribution characteristics of the two kinds of data jumps for the three orbits. Orbit 4954 represents the jump phenomenon features recorded when the four probes were under normal conditions, Orbit 4956 represents the jump phenomenon features recorded under the conditions of the satellite rotated counterclockwise by 90°, and Orbit 4972 represents the jump phenomenon features after the satellite was rotated counterclockwise by 180°. One can observe that the number of gradual-up type of data jumps is higher than that of the straight-

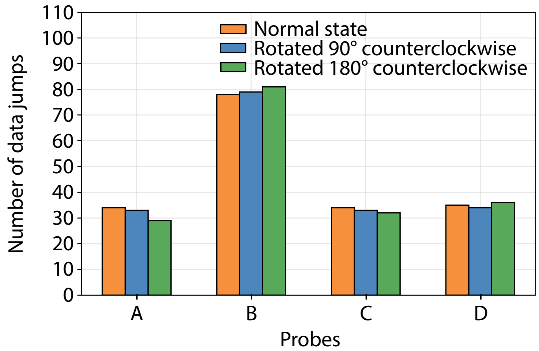

Figure 5. Statistical distribution of data jumps under the normal and experimental states. The horizontal axis represents the four probes, whereas the vertical axis represents the number of data jumps under all three states (denoted by the yellow, blue, and green colors).

down type in all maneuver states. Comparative analysis between the two states after the satellite attitude adjustment and the normal state revealed that both the gradual-up and straight-down jump phenomena were more significant in probe B data compared with the other three probes. No significant changes were observed in the number of both types of data jumps for all four probes across various maneuver states.

The attitude maneuver process of the entire satellite was maintained normally. As shown in Figure 7, after the attitude maneuver, none of the probes showed significant changes in a disturbed state. (Among them, probe A was located within the satellite ion wake region during the yaw 90° maneuver, and probe D was situated in a position very similar to that of probe B under normal flight conditions during the yaw 180° maneuver). The phenomena of data jumps in the low-latitude region for probe B persisted across all maneuver states, whereas no significant interference jumps were present for probes A or D under various maneuver states. Therefore, the experimental results indicated no direct correlation between the disturbance phenomenon of probe B on satellite CSES-01's EFD and the outstretched layout configuration.

3.2 Comparison with the Revisiting Orbits

To exclude contingency factors and more accurately assess the validity and reliability of the experimental results, we selected the revisiting orbits for Orbits 4956 and 4972, which were Orbits 5032 and 5048, respectively. The data from these two revisiting orbits were collected from December 30 to 31, 2018. We focused on the statistical characteristics of waveform data jumps and types across the four probes in the revisiting orbits. As shown in Figure 8, the horizontal axis represents the four probes, whereas the vertical axis represents the number of waveform data jumps.

According to the statistical results presented in Figure 8, note that no significant changes occurred in the data jump phenomena between the two revisiting orbits and the two experimental states for the four selected data features. Through comparative analysis of the four probes, it was evident that the data jump phenomenon in probe B was more pronounced compared with those of the other three probes in both the previous revisiting orbit data and the experimental state orbit data. This result further indicated that the probes did not undergo any notable disturbances during the experimental states. The jump phenomenon in probe B remained consistent across all maneuver states in the revisiting orbit data, whereas probes A, C, and D did not exhibit

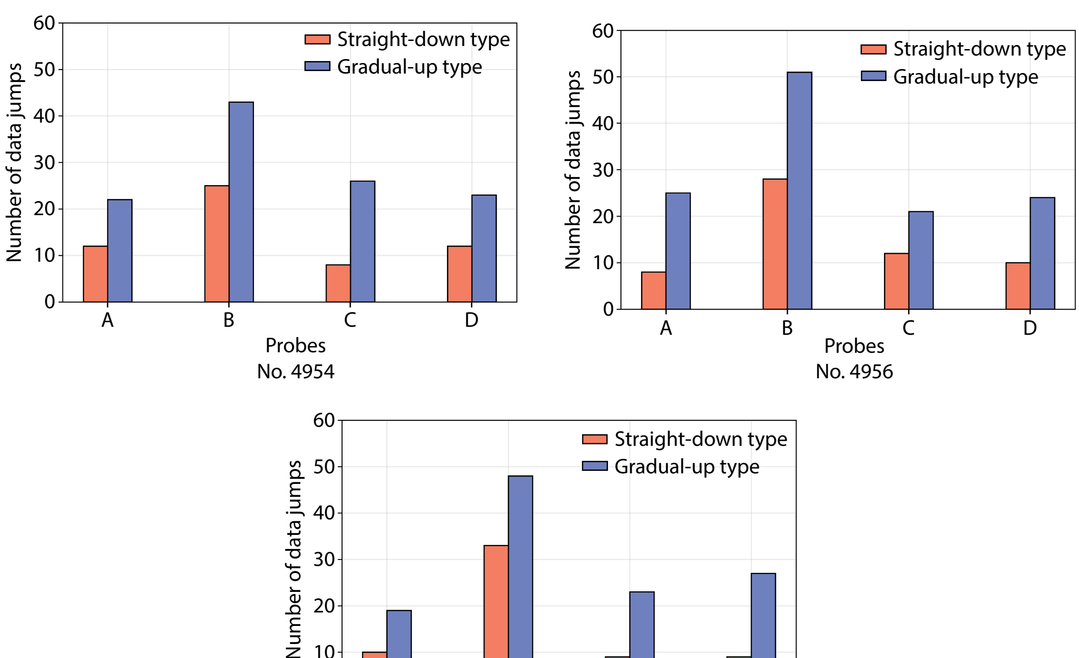

Figure 6. Two kinds of data jump events recorded by three orbits (straight-down and gradual-up types).

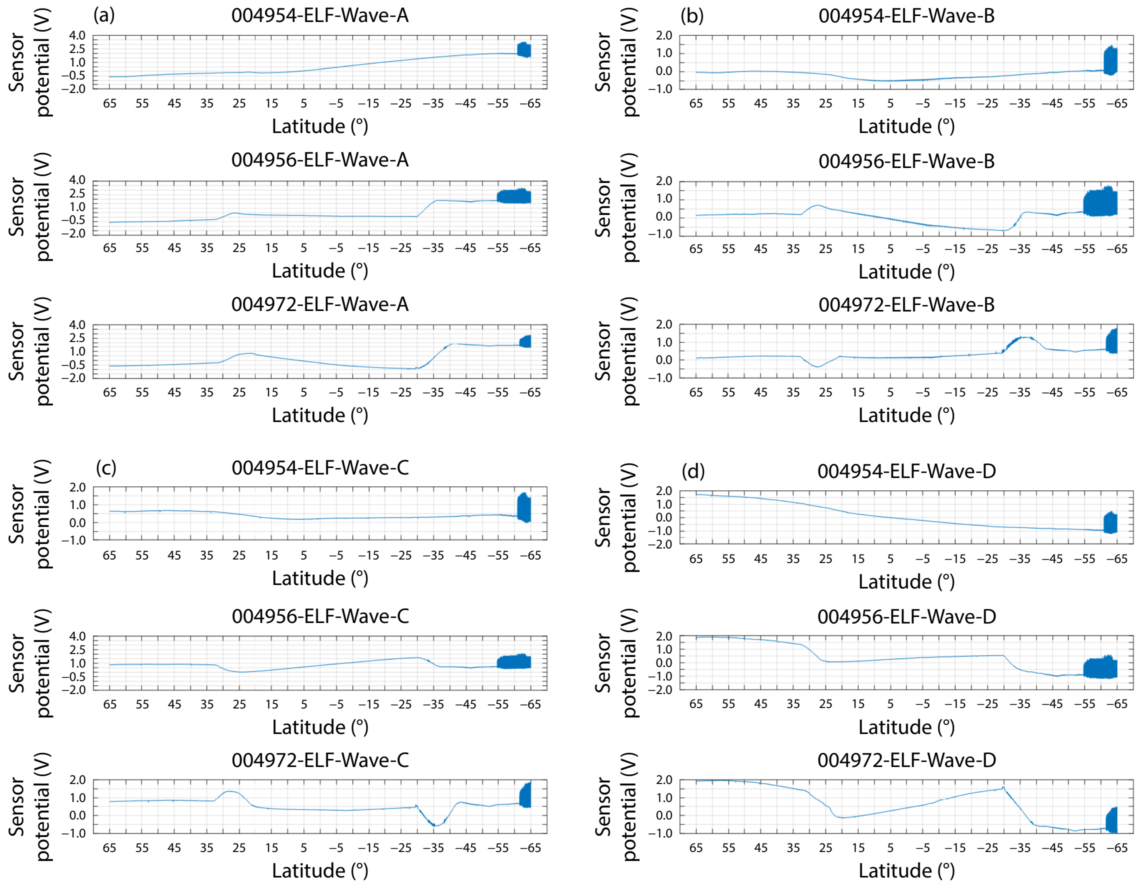

Figure 7. Variation curves of surface potential on probes. (a–d) Surface potential variation curves for probes A, B, C, and D, respectively, where the top panel corresponds to the normal state, the middle panel to a yaw of 90°, and the bottom panel to a yaw of 180°.

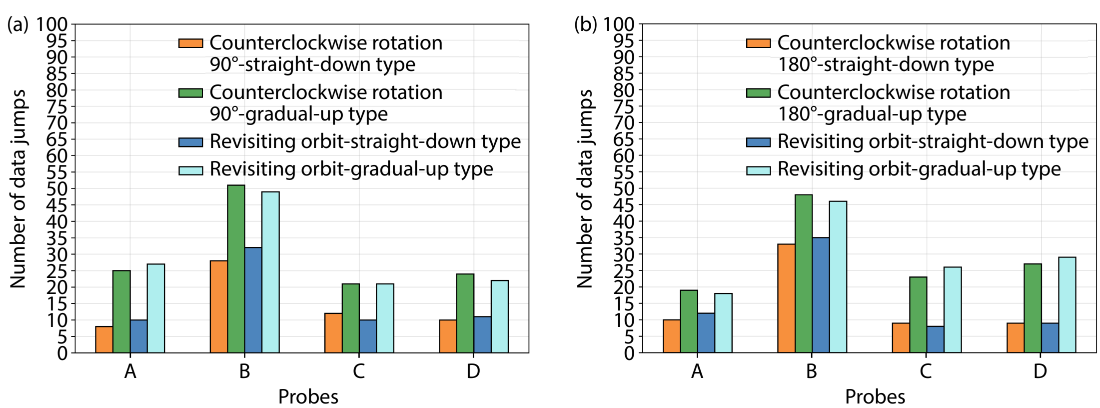

Figure 8. Comparative statistical chart of data jump characteristics for Experiment 1 and Experiment 2 and their corresponding revisiting orbit data.

any significant data jump phenomena in the revisiting orbits for various maneuver states.

4. Discussion

Spatial electric field detection is crucial for studying the physical processes of near-Earth space because it affects satellite stability and communication signal propagation. The double-probe and electron drift methods are commonly used as electric field detection techniques. The double-probe method is mature and reliable, with a wide measurement range, whereas the electron drift method can provide supplementary verification. The detection principle of double-probe detection is that the potential difference between the probes reflects the potential difference in the surrounding plasma environment, and three-dimensional electric field measurement can be achieved through reasonable probe distribution. The spherical probe is a sensitive component, and its surface photoelectric characteristics affect the measurement accuracy of the double-probe method. Circuit noise is the main factor affecting the technical indicators of domestic detectors (Wang YL et al., 2015; Li C et al., 2016; Ma MJ et al., 2017).

The satellite performed a 90° counterclockwise yaw maneuver to avoid the wake region of probe B, thereby verifying whether the disturbed state had improved. After the entire satellite performed a 180° yaw maneuver, probe B was positioned on the ram side of the satellite. During the 90° yaw maneuver, probe A was located within the ion wake region of the satellite, whereas probe C was positioned in a location very similar to probe B during normal flight when the 180° yaw maneuver was performed. The characteristics of data jump phenomena for spherical probes A, B, and C in the normal and two experimental states are shown in Figure 9.

According to the analysis of Figure 9, no significant differences were observed in the data jump characteristics of probes A, B, and C under various states. However, probe B had the most data jumps compared with A and C. In addition, under the two experimental conditions, probe B exhibited more pronounced jump characteristics. This result indicates that the data jump phenomenon of spherical probe B was independent of its spatial location, thus ruling out the influence of the wake effect.

In Experiment 1, the position of spherical probe B was the same as that of spherical probe D in the normal state; in Experiment 2, the position of probe B was the same as that of probe C in the normal state. We defined the positions of probes A, B, C, and D relative to the satellite in the normal state as 1, 2, 3, and 4, respectively. The spatial position numbers in the experimental states are shown in Table 2. Further exploration was conducted on the data jump characteristics of the probes in different spatial positions. Figure 10 illustrates the data jump characteristics of the probes in four spatial positions under both experimental and normal states.

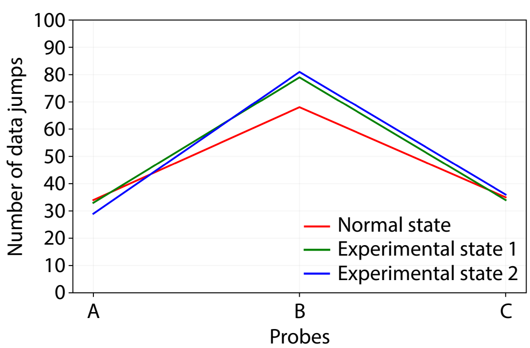

Figure 9. Comparison of data jumps in probes A, B and C located at the satellite's tail during the experimental process.

In the observations of Figure 10a, we noticed that under normal conditions, when the probe was located at position 2, its data jump characteristics exhibited significant differences compared with position 4 in Experiment 1. In contrast, probes at positions 1 and 3 did not show any noticeable changes. Furthermore, as observed in Figure 10b, the probe at position 2 under normal conditions and at position 3 in Experiment 2 also demonstrated notable data jump features, whereas the probes at positions 1 and 4 maintained relatively stable responses. By comparing these experimental results, we could more accurately assess the validity and reliability of the outcomes. The analysis indicated that under various states, none of the probes exhibited apparent changes influenced by the data jump characteristics. Notably, probe B displayed the most prominent data jump characteristics regardless of its location. In contrast, probes A, C, and D did not show any significant data jump phenomena under all tested maneuver conditions. This discovery not only confirms the reliability and stability of the chosen model methodology but also provides a solid foundation for further research and applications.

5. Conclusions

Research on the satellite's attitude maneuvers and data from the EFD's four spherical probes revealed that probe B consistently exhibited data jump phenomena, with a more significant disturbance compared with probes A, C, and D. Despite these anomalies, the overall performance of the probes remained consistent

Table 2. Correspondence between the spatial position numbers and probe numbers.

Spatial position	Normal state probe	Experiment state 1 probe	Experiment state 2 probe
Position 1	A	C	D
Position 2	B	A	C
Position 3	C	D	B
Position 4	D	B	A

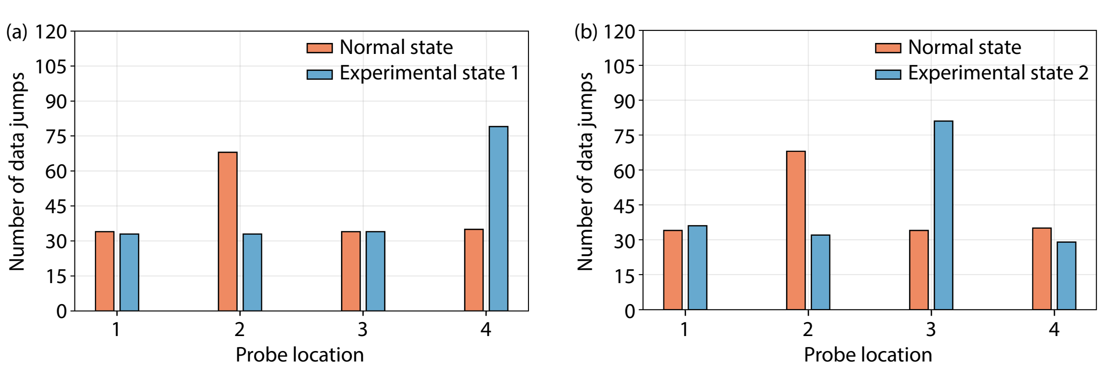

Figure 10. Statistical chart of data jump characteristics for the spatial positions of the four probes.

throughout the experiments, without significant changes observed in the revisiting orbit data for the selected data features. It can be said that the plasma wake effect did not affect the probes and that the probes maintained their measurement accuracy and stability.

The experimental results demonstrated no clear correlation between the disturbance phenomenon of probe B and the satellite's outstretched layout configuration. The attitude maneuver was maintained normally, and the disturbed state did not show significant improvement. The data jump phenomenon in probe B persisted across all maneuver states, whereas probes A and D showed no significant interference jumps under various maneuver states. These findings suggest that the spatial electric field vector data obtained from these probes could still effectively reflect spatial electromagnetic information, despite the abnormalities observed in probe B. The study indicates that the satellite's plasma wake effect and the outstretched layout configuration did not significantly affect the performance of the probes. Although probe B exhibited data jump phenomena, its performance remained relatively stable, and the probes maintained their measurement accuracy and stability.

Acknowledgments

This work made use of data from the CSES mission, a project funded by the China National Space Administration (CNSA) and China Earthquake Administration (CEA). This work was supported by the National Key R&D Program of Intergovernmental Cooperation in Science and Technology (Grant No. 2023YFE0117300); the International Space Science Institute (ISSI in Bern, Switzerland, and ISSI-BJ in Beijing, China), supporting International Team 23-583 led by Dedalo Marchetti and Essam Ghamry; the Hebei Province Graduate Professional Degree Excellent Teaching Case (Library) Construction Project (Grant No. KCJPZ2023060), and the Open Fund for the Key Laboratory of Seismic Disaster Instruments and Monitoring Technology in Hebei Province (Grant No. FZ224104). We acknowledge the CSES Scientific Mission Center for providing data (the English version of https://www.leos.ac.cn/).

References

Bai, Y. D., Liu, J. P., Huang, L., Bai, J. H., and Che, X. H. (2021). Analysis of two convolutional neural networks for map image recognition. *Sci. Surv. Mapp. (in Chinese)*, *46*(11), 126–134. https://doi.org/10.16251/j.cnki.1009-2307.2021.11.018

Berthelier, J. J., Godefroy, M., Leblanc, F., Malingre, M., Menvielle, M., Lagoutte, D., Brochot, J. Y., Colin, F., Elie, F., … Pfaff, R. (2006). ICE, the electric field experiment on DEMETER. *Planet. Space Sci.*, *54*(5), 456–471. https://doi.org/10.1016/j.pss.2005.10.016

Bi, J. Y., and Li, L. (2018). Simulations of the spacecraft charging and wake effects in the solar wind. *Chin. J. Space Sci. (in Chinese)*, *38*(6), 909–914. https://doi.org/10.11728/cjss2018.06.909

Consolini, G., Quattrociocchi, V., D'Angelo, G., Alberti, T., Piersanti, M., Marcucci, M. F., and De Michelis, P. (2021). Electric field multifractal features in the high-latitude ionosphere: CSES-01 observations. *Atmosphere*, *12*(5), 646. https://doi.org/10.3390/ATMOS12050646

Diego, P., Huang, J. P., Piersanti, M., Badoni, D., Zeren, Z. M., Yan, R., Rebustini, G., Ammendola, R., Candidi, M., … Picozza, P. (2021). The electric field detector on board the China Seismo Electromagnetic Satellite—In-orbit results and validation. *Instruments*, *5*(1), 1. https://doi.org/10.3390/instruments5010001

Fuselier, S. A., and Lewis, W. S. (2011). Properties of near-earth magnetic reconnection from in-situ observations. *Space Sci. Rev.*, *160*(1-4), 95–121. https://doi.org/10.1007/s11214-011-9820-x

He, K. M., Zhang, X. Y., Ren, S. Q., and Sun, J. (2016). Deep residual learning for image recognition. In *Proceedings of 2016 IEEE Conference on Computer Vision and Pattern Recognition* (pp. 770–778). Las Vegas, Nevada: IEEE. https://doi.org/10.1109/CVPR.2016.90

Hu, Y. P., Zhima, Z. R., Huang, J. P., Zhao, S. F., Guo, F., Wang, Q., and Shen, X. H. (2020). Algorithms and implementation of wave vector analysis tool for the electromagnetic waves recorded by the CSES satellite. *Chin. J. Geophys. (in Chinese)*, *63*(5), 1751–1765. https://doi.org/10.6038/cjg2020N0405

Huang, J. P., Shen, X. H., Zhang, X. M., Lu, H. X., Tan, Q., Wang, Q., Yan, R., Chu, W., Yang, Y. Y., … Xu, S. (2018a). Application system and data description of the China Seismo-Electromagnetic Satellite. *Earth Planet. Phys.*, *2*(6), 444–454. https://doi.org/10.26464/epp2018042

Huang, J. P., Lei, J. G., Li, S. X., Zhima, Z. R., Li, C., Zhu, X. H., and Yu, W. H. (2018b). The Electric Field Detector (EFD) onboard the ZH-1 satellite and first observational results. *Earth Planet. Phys.*, *2*(6), 469–478. https://doi.org/10.26464/epp2018045

Huang, J. P., Li, Z. Y., Li, Z., Li, W. J., Conti, L., Lu, H. X., Zhou, N., Han, Y., Liu, H. J., … Shen, X. H. (2023). Automatic identification and statistical analysis of data steps in electric field measurements from CSES-01 satellite. *Remote Sens.*, *15*(24), 5745. https://doi.org/10.3390/rs15245745

Jiang, C. H., and Zhao, Z. Y. (2008). Computer simulation on the spacecraft charging. *Spacec. Environ. Eng. (in Chinese)*, *25*(2), 143–147. https://doi.org/10.3969/j.issn.1673-1379.2008.02.010

Kavitha, M., Gayathri, R., Polat, K., Alhudhaif, A., and Alenezi, F. (2022). Performance evaluation of deep e-CNN with integrated spatial-spectral features in hyperspectral image classification. *Measurement*, *191*, 110760. https://doi.org/10.1016/j.measurement.2022.110760

Krizhevsky, A., Sutskever, I., and Hinton, G. E. (2017). ImageNet classification with deep convolutional neural networks. *Commun. ACM*, *60*(6), 84–90. https://doi.org/10.1145/3065386

Li, C., Wang, Z. L., Ma, M. J., Lei, J. G., and Xue, D. T. (2016). Photoelectric characteristics of coatings on spherical sensor for space electric field detection. *Chin. J. Vac. Sci. Technol. (in Chinese)*, *36*(2), 223–228. https://doi.org/10.13922/j.cnki.cjovst.2016.02.17

Liu, S. H., Hu, X. F., Yuan, Q. Y., and Xie, X. N. (2019). Research progress in charging–discharging effects and protection of spacecraft. *High Voltage Eng. (in Chinese)*, *45*(7), 2108–2118. https://doi.org/10.13336/j.1003-6520.hve.20190628007

Liu, Z., Lei, J. G., Ma, M. J., and Li, C. (2021). Sensor design and space application research of spaceborne electric field instrument. *Mach. Des. Manuf. Eng. (in Chinese)*, *50*(3), 96–100. https://doi.org/10.3969/j.issn.2095-509X.2021.03.021

Ma, M. J., Lei, J. G., Li, C., Zong, C., Li, S. X., Liu, Z., and Cui, Y. (2017). Characteristic of space electric field and its detection technology. *Vac. Cryog. (in Chinese)*, *23*(1), 25–30. https://doi.org/10.3969/j.issn.1006-7086.2017.01.005

Ma, M. J., Lei, J. G., Li, C., Li, S. X., Zong, C., Liu, Z., and Cui, Y. (2018). Design optimization of Zhangheng-1 space electric field detector. *Chin. J. Vac. Sci. Technol. (in Chinese)*, *38*(7), 582–589. https://doi.org/10.13922/j.cnki.cjovst.2018.07.06

Shen, X. H., Zhang, X. M., Yuan, S. G., Wang, L. W., Cao, J. B., Huang, J. P., Zhu, X. H., Piergiorgio, P., and Dai, J. P. (2018). The state-of-the-art of the China Seismo-Electromagnetic Satellite mission. *Sci. China Technol. Sci.*, *61*(5), 634–642. https://doi.org/10.1007/s11431-018-9242-0

Tian, L. C., Shi, H., Li, J., and Zhang, T. P. (2012). Simulation of spacecraft surface charging and active control of spacecraft surface potential. *Spacecr. Environ. Eng. (in Chinese)*, *29*(2), 144–149. https://doi.org/10.3969/j.issn.1673-1379.2012.02.006

Ukhorskiy, A. Y., Mauk, B. H., Fox, N. J., Sibeck, D. G., and Grebowsky, J. M. (2010). Radiation belt storm probes: Resolving fundamental physics with practical consequences. *J. Atmos. Sol. Terr. Phys.*, *73*(11-12), 1417–1424. https://doi.org/10.1016/j.jastp.2010.12.005

Wang, L., and Qin, X. G. (2002). Researches on the evaluating test methods of space material's surface charging/discharging characteristics. *Vac. Cryog. (in Chinese)*, *8*(2), 83–87. https://doi.org/10.3969/j.issn.1006-7086.2002.02.004

Wang, Y. L., Lei, J. G., Ma, M. J., Cui, Y., and Li, S. X. (2015). The analysis of circuit noise on space EFD. *Space Electron. Technol. (in Chinese)*, *12*(3), 88–94. https://doi.org/10.3969/j.issn.1674-7135.2015.03.015

Yang, D. H., Zhima, Z. R., Wang, Q., Huang, J. P., Wang, X. Y., Zhang, Z. X., Zhao, S. F., Guo, F., Cheng, W. L., … Shen, X. H. (2022). Stability validation on the VLF waveform data of the China-Seismo-Electromagnetic Satellite. *Sci. China Technol. Sci.*, *65*(12), 3069–3078. https://doi.org/10.1007/S11431-022-2059-8

Yang, F., Shi, L. Q., Liu, S. Q., and Gong, J. C. (2011). Surface charging simulation of LEO spacecraft. *Chin. J. Space Sci. (in Chinese)*, *31*(4), 509–513. https://doi.org/10.11728/cjss2011.04.509

Yang, J. Chen, X. X., Zhou, J., and Xia, S. H. (2010). Investigation of the influence of wake effect on plasma sheath. *J. Astronaut. (in Chinese)*, *31*(2), 531–535. https://doi.org/10.3873/j.issn.1000-1328.2010.02.036

Yang, Y. Y., Zhima, Z. R., Shen, X. H., Chu, W., Huang, J. P., Wang, Q., Yan, R., Xu, S., Lu, H. X., and Liu, D. P. (2020). The first intense geomagnetic storm event recorded by the China Seismo-Electromagnetic Satellite. *Space Wea.*, *18*(1), e2019SW002243. https://doi.org/10.1029/2019SW002243

Yuan, Q. Y., and Sun, Y. W. (2015). Surface charging simulation of spacecraft in different orbits. *J. Hebei Norm. Univ. (Nat. Sci.) (in Chinese)*, *39*(1), 38–45. https://doi.org/10.13763/j.cnki.jhebnu.nse.2015.01.007

Zeiler, M. D., and Fergus, R. (2014). Visualizing and understanding convolutional networks. In *Proceedings of the 13th European Conference on Computer Vision 2014* (pp. 818–833). Zurich, Switzerland: Springer. https://doi.org/10.1007/978-3-319-10590-1_53

Zhima, Z. R., Huang, J. P., Shen, X. H., Xia, Z. Y., Chen, L. J., Piersanti, M., Yang, Y. Y., Wang, Q., Zeng, L., … Guo, F. (2020). Simultaneous observations of ELF/VLF rising-tone quasiperiodic waves and energetic electron precipitations in the high-latitude upper ionosphere. *J. Geophys. Res.: Space Phys.*, *125*(5), e2019JA027574. https://doi.org/10.1029/2019JA027574

Zhima, Z. R., Yan, R., Lin, J., Wang, Q., Yang, Y. Y., Lv, F. X., Huang, J. P., Cui, J., Liu, Q. Q., … Shen, X. H. (2022a). The possible seismo-ionospheric perturbations recorded by the China-Seismo-Electromagnetic Satellite. *Remote Sens.*, *14*(4), 905. https://doi.org/10.3390/RS14040905

Zhima, Z. R., Zhou, B., Zhao, S. F., Wang, Q., Huang, J. P., Zeng, L., Lei, J. G., Chen, Y., Li, C., … Shen, X. H. (2022b). Cross-calibration on the electromagnetic field detection payloads of the China Seismo-Electromagnetic Satellite. *Sci. China Technol. Sci.*, *65*(6), 1415–1426. https://doi.org/10.1007/S11431-021-1965-2